

## NON-INVASIVE MEASUREMENTS OF TRANSPARENT FIBRES

Grzegorz Świrniak

Wrocław University of Science and Technology, Faculty of Electronics, B. Prusa 53/55, 50-317 Wrocław, Poland  
(✉ [grzegorz.swirniak@pwr.edu.pl](mailto:grzegorz.swirniak@pwr.edu.pl), +48 71 320 6228)

### Abstract

This paper presents a non-invasive measurement method for simultaneous characterization of diameter and refractive index of transparent fibres. The method is based on scattering of a polychromatic beam of light by a side-illuminated fibre under study. Both quantities of interest are inversely calculated from the scattering far-field region in the vicinity of the primary rainbow. The results of practical measurements are examined with the use of a novel optical system for laboratory-level tests. An analysis of prediction errors for 20–120  $\mu\text{m}$  thick fibres having various refractive indices helps to assess the outcome of the measurement data. The results show a clear route to improve the measurement process in on-line industrial process control.

Keywords: fibre characterization, scattering measurements, inverse scattering.

© 2020 Polish Academy of Sciences. All rights reserved

## 1. Introduction

Transparent (glass or polymer) micron-sized fibres are commonly used for fabrication of optically transparent composite materials. Such modern composites provide excellent optical transparency and low image distortion while exhibiting superior mechanical properties, which make them perfect for the production of airplane windshields, motorcycle helmets, composite lenses, *etc.* Fibrous reinforcements comprise various combinations of fibres incorporated in an epoxy matrix material. Optical transparency of a composite (up to about 90% [1–3]) is achieved by matching the refractive index of a glass fibre and a polymer matrix (approximately to within  $\pm 0.002$  for a PMMA matrix [4, 5]). Furthermore, the light transmittance of the composite increases with the fibre diameter and decreases with increasing the volume percentage of unidirectionally arranged fibres [3]. A technical verification of the fibre characteristics such as the diameter and refractive index during the production process (fibre drawing) is thus extremely important from the viewpoint of composite technology.

Optical non-imaging techniques are routinely used for high-precision non-contact gauging of transparent fibres. The most common are laser diffractometry [6] and laser beam scanning [7], both offering the possibility to determine the outer characteristics of a fibre under test. Fundamentally, these techniques are based on the contrast mechanism (where the fibre edge

affects the measurements). This simple mechanism appears to be inadequate for characterizing transparent fibres, since the “edge pattern” is affected by the portion of light passing through, so that recovering the fibre characteristics is impractical.

The measurement method presented in this manuscript aims at non-contact and simultaneous gauging of the diameter and refractive index of optically transparent, micron-sized fibres used in optically transparent composites. The method can be also applied to obtain cladding characteristics in single-mode optical fibres. High-precision refractive index and diameter estimates are based on the far-field primary rainbow pattern, which occurs due to scattering of a polychromatic beam of light by the fibre under test.

As precise quantitative understanding of the rainbow mechanism is necessary and the inverse problem (enabling to interpret data by relating the optical field back to the properties of interest in the object, see *e.g.* [8–10]) is decidedly non-trivial, the paper initially discusses modelling of scattered fields in the vicinity of the rainbow pattern. Central to this discussion is the fact that the coherence properties of the incident beam can be adjusted specifically to improve the stability of the inverse problem. Moreover, the scattering system can be modelled with the simpler Airy’s theory of rainbows rather than the full solution based on Maxwell’s equations.

The results of practical measurements in this study are examined by using a novel optical system for laboratory-level dynamic gauging of transparent fibres. In particular, it is explored how the scattering data and the fibre estimates (*i.e.*, refractive index and diameter) depend on the fibre ellipticity (which is not accounted for by scattering models). As the rainbow imaging with polychromatic beams is rather a non-standard method, a detailed description of the system setup is provided.

The final part of this manuscript provides a statistical analysis of prediction errors for the diameter and refractive index estimates.

## 2. Rainbows produced by transparent fibres

### 2.1. Scattering of polychromatic light beams

Electromagnetic scattering by transparent particles with a high-degree of rotational symmetry (*e.g.* spheres, cylinders, spheroids, *etc.*) and with the refractive index greater than that of the surrounding medium, can produce a series of rainbows. Depending on the number of internal reflections of light, multiple rainbows can be observed in the far field. For example, scattering of sunlight by water droplets usually produces a strong, primary rainbow (caused by light that has been subjected to one internal reflection) and, in favourable conditions, a much weaker secondary rainbow (two internal reflections). Multiple rainbows of the same order (*e.g.* multiple primary rainbows) can be also seen when light travels through inhomogeneous (layered) particles [11–13]. Thus, the light affected by a particle carries a lot of information about the particle’s shape and composition.

Figure 1 shows geometry of the scattering. Numerical predictions of polychromatic rainbows in this study assume that the illuminated fibre can be modelled as an infinitely long, axisymmetric and homogeneous cylinder, which is characterized by a complex wavelength-dependent index of refraction:

$$m(\lambda) = \left[ 1 + \sum_{i=1}^3 A_i \lambda^2 / (\lambda^2 - \ell_i^2) \right]^{1/2} + i\kappa, \quad (1)$$

where  $A_i$ ,  $\ell_i$  are Sellmeier coefficients [14] and  $\kappa$  describes the attenuation of electromagnetic wave in the fibre. The incident wave field is considered as the vector superposition of the number

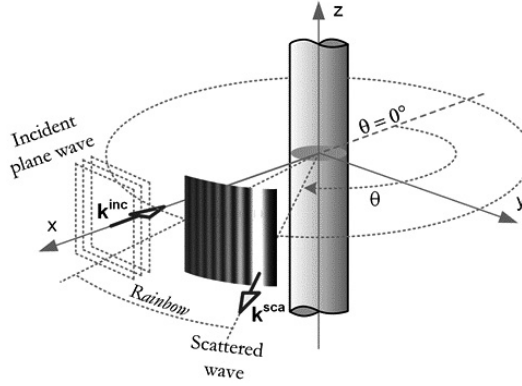


Fig. 1. Geometry of the transparent fibre illuminated by beam of light propagating in the  $-x$  direction.

of mutually incoherent monochromatic fields propagating in the same direction and having a continuous distribution of angular frequencies ranging within  $(\omega_{\min}, \omega_{\max})$ :

$$E^{inc}(xt) = \sum_{n=1}^N E_n^{inc}(t) \exp(-ik_n^{inc}x - i\omega_n t), \quad (2)$$

where  $E_n^{inc}(t)$  is the complex amplitude of electric field which fluctuates randomly in time with its period long compared to the complex temporal term  $\exp(-i\omega_n t)$ , and  $k_n^{inc}$  is a (real-valued) wave vector. The transformation of the incident monochromatic wave  $E_n^{inc}$  into the scattered wave  $E_n^{sca}$  upon its interaction with the fibre is treated rigorously as a separate event with the use of *separation-of-variables solution* (SVM) of Maxwell's equations, where the scattered field is expanded into a series of cylindrical vector wavefunctions  $M_n, N_n$  [15, 16]:

$$E_n^{sca}(\mathbf{r}) = - \sum_{m=-\infty}^{\infty} E_m \left( b_{mI} N_m^{(3)} + ia_{mI} M_m^{(3)} \right). \quad (3)$$

The expansion coefficients of the scattered field  $a_{mI}, b_{mI}$  are derived numerically by applying boundary conditions to the tangential field components on the fibre's surface [17]. The complex magnetic field  $H_n^{sca}(\mathbf{r})$  is obtained by using the Maxwell's curl  $E$  equation. Assuming that the interaction of light with the fibre is linear, the time-averaged Poynting vector of the scattered electromagnetic field at point  $\mathbf{r}$  in space can be obtained by applying an additivity rule:

$$\langle\langle S^{sca}(\mathbf{r}, t) \rangle\rangle = \text{Re} \sum_{n=1}^N S_n^{sca}(\mathbf{r}), \quad (4)$$

where  $\langle\langle \dots \rangle\rangle$  denotes averaging over a long time interval and  $S_n^{sca}$  is the complex Poynting vector of the  $n^{\text{th}}$  monochromatic component comprising the incident field:

$$S_n^{sca}(\mathbf{r}) = \frac{1}{2} E_n^{sca}(\mathbf{r}) \times [H_n^{sca}(\mathbf{r})]^*, \quad (5)$$

with  $(*)$  denoting the complex conjugate. The scattered intensity in the far field,  $I^{sca}(\mathbf{r})$ , is the magnitude of the time-averaged Poynting vector.

Figure 2a shows a graph of scattered intensity as a function of scattering angle for a transparent silica fibre with a diameter of 100  $\mu\text{m}$ , illuminated by a polychromatic beam of light. The calculations assumed Gaussian distribution of the emission line of the incident light with the peak wavelength  $\lambda_0 = 0.6328 \mu\text{m}$  and bandwidth FWHM (full width at half maximum), corresponding to the coherence length  $l_c = (2 \ln(2)/\pi m_0)^{1/2} \times (\lambda_0^2/\text{FWHM})$ , where  $m_0 = 1$  is the refractive index of the surrounding medium. The electric vector of the incident beam of light oscillates along the fibre main axis (transverse magnetic or TM polarization). If the electric field is polarized perpendicularly to the cylinder axis (the transverse electric or TE case), the intensity of the rainbow is much weaker, as the Brewster condition for light refraction inside the fibre is met [18]. In Fig. 2a the primary rainbow pattern is located at scattering angles of around  $150^\circ - 175^\circ$ . The intricate details of the plots indicate that the rainbow has a complicated nature. With increasing the FWHM, the high-frequency structures (or “speckles”) become less pronounced as the optical paths taken by the interfering scattered waves at  $\mathbf{r}$  differ by more than the coherence length  $l_c$  of the light (the “smoothing effect”) [19]. Fig. 2b shows that the fibre diameter mainly affects the angular spacing between rainbow extrema. The smoothing effect clearly depends on the fibre size, as the optical paths of several monochromatic waves contributing to scattering vary with particle geometry. Finally, Fig. 2c evidences that the angular shifts of the rainbow pattern correspond to the changes in the refractive index. These observations help to choose a proper strategy for retrieving the fibre characteristics from the measurement results, see Subsection 2.2.

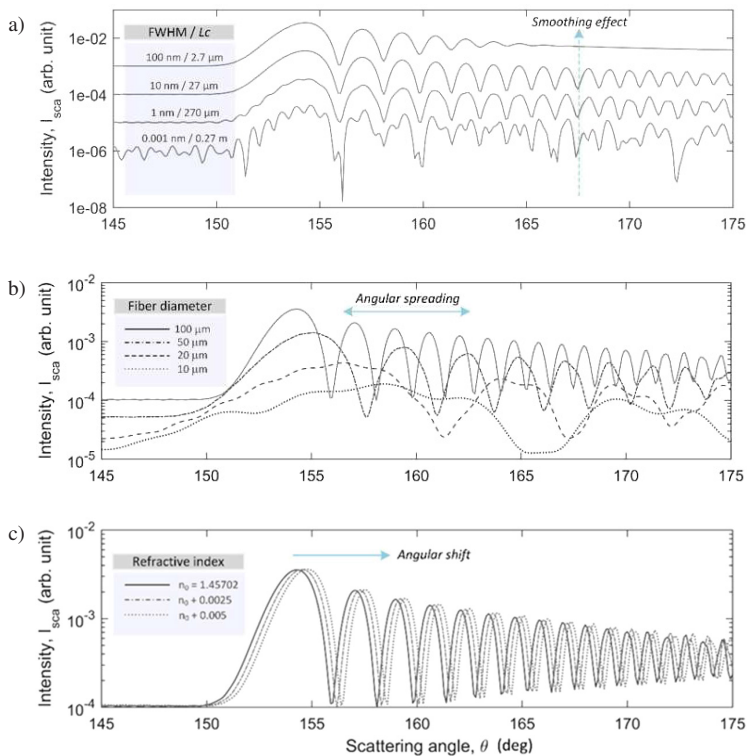


Fig. 2. Plots of scattered intensity as a function of scattering angle for a transparent silica fibre illuminated by a polychromatic beam of light ( $\lambda_0 = 633 \text{ nm}$ ): a) the effect of the spectral bandwidth (FWHM) of the incident beam of light; the fibre diameter  $d = 100 \mu\text{m}$ ; b) the effect of the fibre diameter; FWHM = 15 nm; c) the effect of the refractive index of the fibre;  $d = 100 \mu\text{m}$ , FWHM = 15 nm.

With monochromatic illumination, *morphology-dependent resonances* (MDRs) may occur for various combinations of the diameter (or shape, in general) and refractive index of transparent and axisymmetric particles [20, 21]. These complex distortions cannot be predicted in practice (in the presence of noise and small experimental uncertainties) and often render data interpretation useless. The use of polychromatic illumination, however, reduces this detrimental sensitivity of scattering to particle’s morphology [19]. The stability and reliability of measurement results, in turn, are critical for controlling the industrial process control.

## 2.2. Approximate forward and inverse models of scattering

Polychromatic rainbows can be accurately modelled by various simplified models of scattering rather than the full SVM solution [19]. This provides not only a computational simplification but, more importantly, leads to mathematical formulas that are well posed in the sense of Hadamard [22, 23], *i.e.*, small perturbations of the scattering object characteristics (size, composition, *etc.*) produce unique solutions which change continuously with the measurement conditions (in contrast to various measurement techniques based on monochromatic light scattering, see *e.g.* [24–28]).

In this study we use the Airy’s theory of primary rainbow for approximate examinations of scattering [11, 29], albeit augmented with a correction to reduce the approximation error. The far-field intensity pattern is modelled by [19]:

$$I_z^{sca}(\theta, x, n) \propto \text{Ai}^2 \left[ -x^{2/3} \Delta / h^{1/3} (1 + B\Delta) \right], \quad (6)$$

where  $\theta$  is the scattering angle;  $\text{Ai}(z)$  is the Airy’s integral [30];  $x = \pi d / \lambda_0$  is the “size parameter” with  $d$  being the fibre diameter;  $\Delta \equiv \theta - \theta^D$ , and  $\theta^D$  is the angle of a so-called Descartes ray of rainbow (or “rainbow angle”), which is a function of the real-valued index of refraction ( $n$ ) and provides an approximate position of the rainbow in the far field:

$$\begin{aligned} \theta^D &= \pi + 2\theta_i^D - 4\theta_t^D, \\ \cos(\theta_i^D) &= [(n^2 - 1)/3]^{1/2}, \quad \sin(\theta_t^D) = n^{-1} \sin(\theta_i^D). \end{aligned} \quad (7)$$

The correction term  $(1 + B\Delta)$  in (6) improves rainbow predictions. The coefficient  $B$  has been introduced by Nussenzweig in the framework of the *complex angular momentum* (CAM) theory of rainbow [31]:

$$\begin{aligned} B &= [(875c^6 - 1257c^4 + 657c^2 + 45)/8640(cs)^3], \\ s &= [(4 - n^2)/3]^{1/2}, \quad c = [(n^2 - 1)/3]^{1/2}. \end{aligned} \quad (8)$$

Finally,  $h$  in (6) is a dimensionless measure of the curvature of the wave-front near the rainbow angle:

$$h = 9(4 - n^2)^{1/2} / 4(n^2 - 1)^{3/2}. \quad (9)$$

Figure 3 compares the numerical evaluation of the primary rainbow produced by scattering of polychromatic light with FWHM = 15 nm by a silica fibre with a diameter of 100  $\mu\text{m}$  (solid line), Subsection 2.1, with the Airy’s approximate predictions for scattering of a *monochromatic* wave (dashed line). Although the match is nearly perfect (in terms of peak positions), the approximation quality depends on various experimental conditions, such as particle’s morphology (size, refractive index), incident beam characteristics (central wavelength, FWHM, the angle of incidence), *etc.* [19].

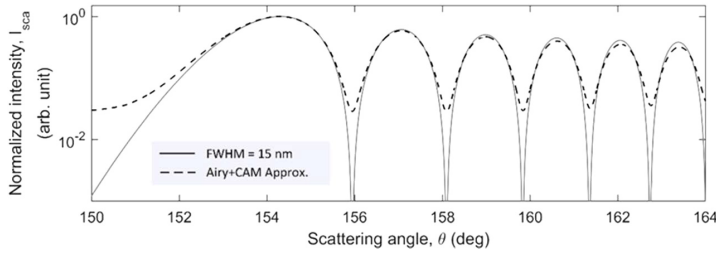


Fig. 3. (solid line): Scattered intensity (log scale) in the vicinity of the primary rainbow for a transparent silica fibre having a diameter of 100  $\mu\text{m}$ , illuminated by a polychromatic beam of light ( $\lambda_0 = 633 \text{ nm}$ , FWHM = 15 nm); (dashed line): Airy's approximation for a polychromatic rainbow ( $\lambda_0 = 633 \text{ nm}$ ).

The inversion algorithm, which aims at reconstructing the fibre refractive index/diameter from the results of scattering measurements, at first step assumes computation of the cladding refractive index on the basis of the absolute positions of rainbow minima/maxima,  $(\theta_i, \theta_j)$  [19]:

$$\Delta_j \Delta_i^{-1} = z_j z_i^{-1} (1 + B \Delta_j)^{-1} (1 + B \Delta_i), \quad (10)$$

where  $\Delta_{i,j} = \theta_{i,j} - \theta^D$  and  $(z_i, z_j)$  are the critical points of the Airy's integral  $\text{Ai}(z)$  at which the rainbow's minima and maxima occur [30]. As (10) has no closed form, it is computed using an iterative procedure. The cladding diameter estimates can be made on the basis of maxima/minima spacing:

$$z_i - z_j = \left( x^{2/3} / h^{1/3} \right) [\Delta_i (1 + B \Delta_i) - \Delta_j (1 + B \Delta_j)]. \quad (11)$$

### 3. Experimental setup

A novel optical system for laboratory-level dynamic gauging of transparent fibres consists of four main parts, as in Fig. 4: illumination optics, collection optics, fibre alignment optics, and an automated measurement platform. Fig. 5 shows a general view of the system.

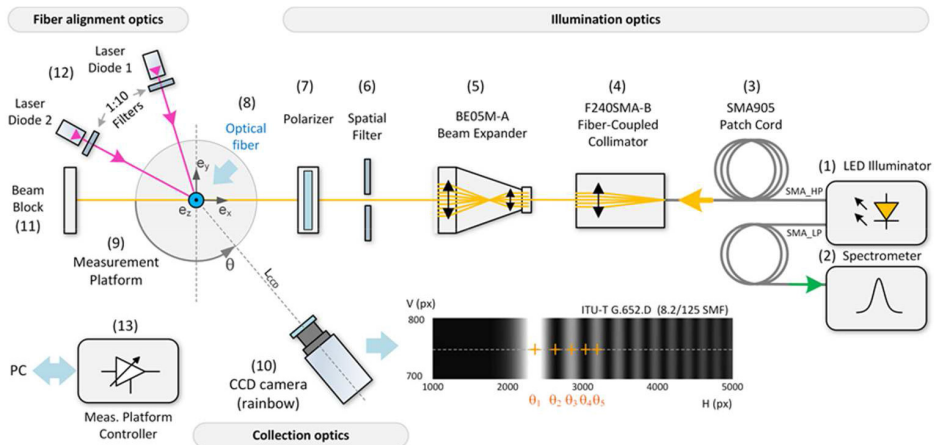


Fig. 4. Experimental system for laboratory-level, non-invasive measurements of transparent fibres [34]. The inset shows a CCD capture of the primary rainbow for a standard single-mode optical fibre.

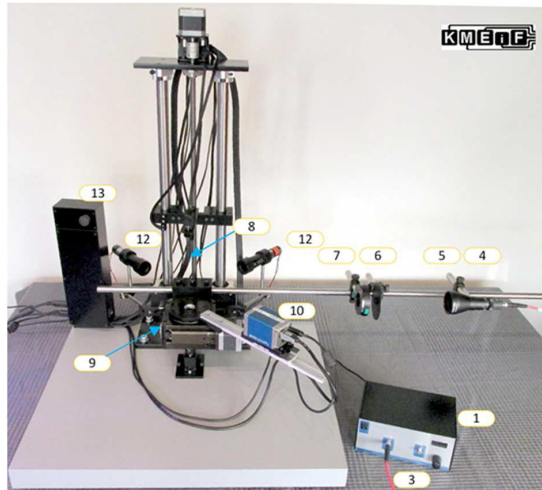


Fig. 5. A general view on the experimental system for non-invasive measurements of transparent fibres (numbers as in Fig. 4).

The system uses a beam of polychromatic light produced by a compact  $150 \times 70 \times 100$  mm ( $5.90 \times 2.76 \times 3.93''$ ) two-channel illuminator (1) of a prototype construction having an output of about 33 mW (radiant flux) [32]. The illuminator consists of a high-power red LED ( $\lambda_0 \approx 630$  nm, FWHM  $\approx 14.5$  nm) that is precisely coupled to an SMA905 termination using a butt-coupling technique for convenient connecting to other optical components. A small amount of light is also delivered to the second SMA905 output used to measure spectral characteristics of the produced radiation (2). The LED is attached to an actively-cooled heat sink. This ensures a good stability of the light output (emission spectrum, luminous flux) as well as enables to shift the dominant wavelength by changing temperature of the LED junction (approx.  $-3$  nm to  $+12$  nm) [33]. The optical power from the LED illuminator is delivered to a fixed focus collimator (4) which contains one factory-aligned aspheric lens to operate at a wavelength of 633 nm. The output from the collimator is then processed by a Galilean beam expander (5) used to further reduce divergence, which will decrease by the same factor as magnification ( $5\times$ ) is increased. The expanded beam goes through a spatial filter (6) which protects the scattering pattern against interference of unwanted background light from the system (speckles, *etc.*) on. A light polarization filter (7) is necessary to select a specific polarization state as various LED structures exhibit either virtually non-polarized or partially polarized output [35]. The resulting beam of light illuminates the fibre under test (8) at a normal angle. The probe volume diameter is about 3 mm. The beam block (11) absorbs unwanted forward scattered radiation. The light scattered by the fibre is collected by a low-noise, high-quantum efficiency, 14-bit camera (10) with a CCD  $1392 \times 1040$  px sensor (Pixelfly, PCO AG). By adjusting the exposure time and gain, it is possible to acquire weak signals with the use of an entire dynamic range. A dedicated software is able to combine multiple images taken at successive angular positions ( $\theta$ ). The fibre alignment optics uses two laser diodes (12) and the CCD to determine various geometric misalignments which vary as the camera rotates. These misalignments result from the fact that the fibre main axis may not coincide with the axis of rotation of the CCD camera [34]. The software attempts to determine these misalignments before each measurement to avoid unwanted data bias.

The fibre under test is mounted on a motorized measurement platform, see Fig. 6. The fibre (i) is attached to two synchronized servomechanisms (ii) which provide a fine rotation  $0-180^\circ$  about the fibre's main axis. The fibre runs vertically through the middle of motorized stage (iii), which provides a common scattering plane for the illumination optics (iv), a CCD camera (v), and two laser diodes (vi) used for the fibre alignment. The illumination optics is precisely positioned on a 50 cm (19.7") long steel rod. The camera is mounted on a rotation arm providing  $\pm 0.01^\circ$  of fine rotation or even  $\pm 0.625E - 3^\circ$  in a micro-step mode. This feature enables a detailed analysis of the scattered far field in a wide range of scattering angles. A long-travel vertical translation stand (vii) accurately positions the motorized stage (iii) along the fibre's axis with a step of  $10\ \mu\text{m}$ . By combining the vertical translation along the length of the fibre with its rotation, it is possible to examine the fibre's *circularity* (which refers to how close to a perfect circle is the fibre's cross-section) as well as its *cylindricity* (*i.e.*, the circularity extended along the main axis of the fibre). Finally, the measurement platform is controlled by a dedicated benchtop motion controller (13 in Fig. 5) enabling to easily integrate it with automated motion control applications. USB connectivity provides easy plug-and-play PC operation. The controller can also operate in the standalone mode using a joystick console for intuitive, tactile, manual positioning of the platform.

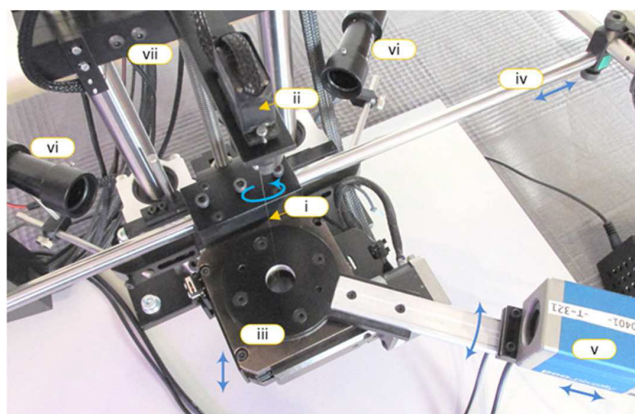


Fig. 6. High-precision measurement platform – provides mounting of the fibre under test and precise, fine positioning for the illumination and collection assemblies [34].

#### 4. Results and discussion

Practical measurements aimed at characterization of a standard single-mode optical fibre SSMF  $8.2/125\ \mu\text{m}$  (ITU-T G.652.D). A small core of the fibre does not affect the far-field primary rainbow features [19]. The peak wavelength of the incident polychromatic beam has been adjusted at 633 nm. Fig. 7 shows typical scattered intensity plots as functions of scattering angle. The seven curves refer to various rotation angles of the fibre relative to the direction of incidence of the light beam, as depicted in the inset of Fig. 7. Since the optical fibre's cross-sections is not circular, the angular position of rainbow varies when the fibre is rotated. Both absolute positions of rainbow peaks as well as distance between any two consecutive peaks (albeit to a much lesser extent) depend on the fibre rotation but, importantly, the rainbow is structurally stable, *i.e.*, it is unaffected by small perturbations in shape or boundary conditions [36, 37].

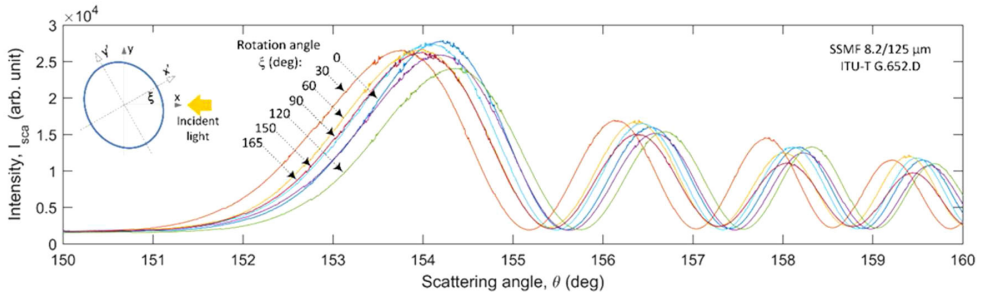


Fig. 7. Plots of scattered intensity in the vicinity of the primary rainbow for a standard single-mode 8.2/125  $\mu\text{m}$  optical fibre (SSMF, ITU-T G.652.D) as a function of fibre rotation angle  $\xi$ .

Figure 8 shows how the fibre orientation affects the refractive index (A) and diameter (B) estimates. The inversion formulas (10) and (11) used the angular positions of the first two maxima as input. The refractive index data points in Fig. 8a follow periodically changes in the orientation angle, which suggests that the fibre's cross-section is elliptical. This sensitivity to the fibre's shape is a consequence of the inversion strategy, which assumes that the refractive index is reconstructed from the absolute positions of rainbow peaks. The mean value of the refractive index is 1.4565, while the standard deviation is close to 0.002. The refractive index measurements agree well with the refractive index of a pure silica ( $\text{SiO}_2$ , cladding material) which is 1.4570 at 633 nm. The diameter dataset from Fig. 8b is overlaid by a noise signal. Note that the diameter formula (11) bases on the angular difference between the positions of two maxima. As both maxima move in a similar way with the rotation angle, as illustrated in Fig. 7, the diameter values are somewhat robust to some un-modelled changes in the fibre's cross-section. A mean value of the cladding diameter predictions is 126.0  $\mu\text{m}$  with a standard deviation of around 1.7  $\mu\text{m}$ . According to ITU-T G.652.D (11/2016) specification for SSMF fibres, the recommended mean cladding diameter is

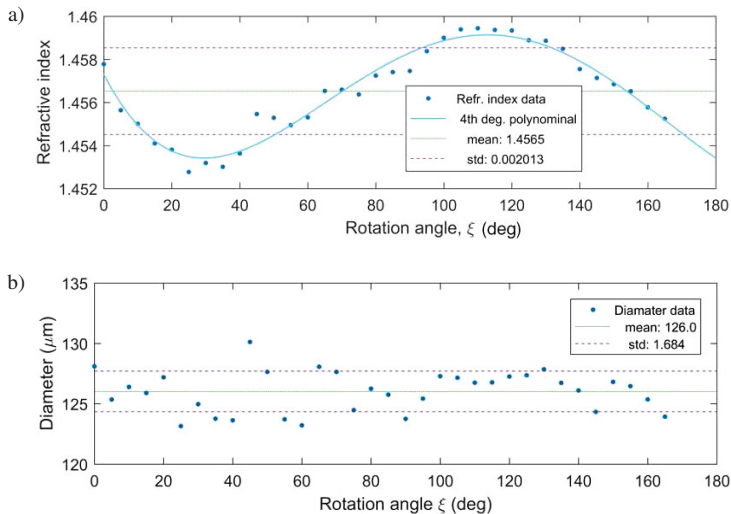


Fig. 8. Refractive index (a) and diameter (b) estimates as functions of the fibre rotation angle (SSMF 8.2/125  $\mu\text{m}$ , ITU-T G.652.D). 34 data points are 5° apart from each other.

125  $\mu\text{m}$  with a tolerance of  $\pm 0.7 \mu\text{m}$ , while the cladding non-circularity should be less than 1%, see Fig. 9. The diameter predictions, therefore, agree with ITU specifications. As the Airy's theory do not account for deviations of the fibre's cross-section from a perfect circle, the mean value from a series of diameter predictions would probably be the measure of the mean fibre diameter, as defined by ITU specifications.

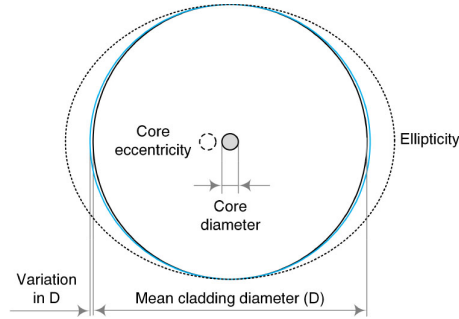


Fig. 9. The geometry of an optical fibre.

For a better understanding of how various small experimental uncertainties affect the fibre estimates, the *root-mean-square* (RMS) errors for the refractive index/diameter data series have been evaluated. The numerical analysis based on a database of 462 synthetic scattering signals evaluated with the use of complex modelling for polychromatic light beams (see Subsection 2.1) for 21 values of the refractive index (1.35–1.5) and 22 values of the diameter (20–120  $\mu\text{m}$ ) of a silica fibre of interest. Each scattering signal has been affected 200 times by noise having a normal distribution with zero mean and standard deviation  $\sigma = 1\%$  of the maximum intensity (a typical value for the CCD camera used in our experimental setup). 200 retrievals of the refractive index and diameter were carried out for each of the synthetic scattering signal differing in noise sequence. Fig. 10 shows plots of RMS errors of the refractive index (a) and diameter (b) estimates

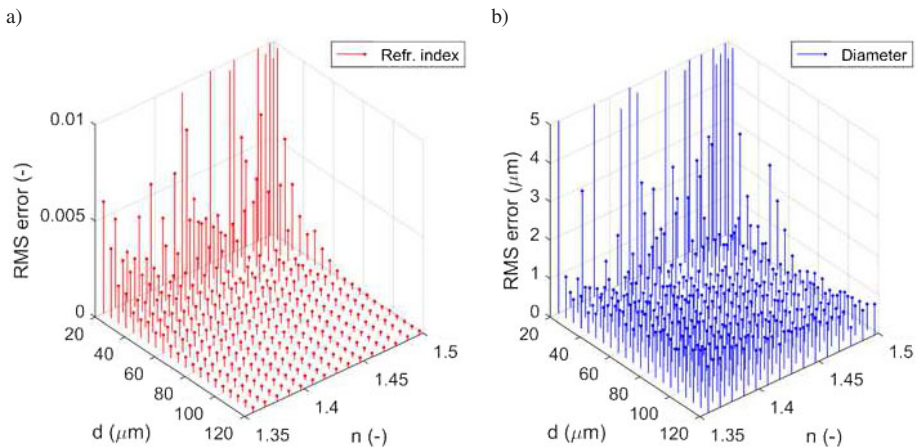


Fig. 10. 3-D plots showing *root-mean-square* error (RMS) of the refractive index (a) and diameter (b) estimates as functions of true values of the parameters being estimated. The scattered intensity contains an additive noise with standard deviation  $\sigma = 1\%$  (see text). The silica fibre under study is illuminated by a beam of polychromatic light with  $\lambda_0 = 633 \text{ nm}$  and FWHM = 15 nm.

as functions of true values of the parameters being estimated. The incident beam has the peak wavelength at 633 nm and the spectral half-width of 15 nm. Figs. 11a and 11b are equivalent to Figs. 10a and 10b, respectively, except that FWHM = 40 nm.

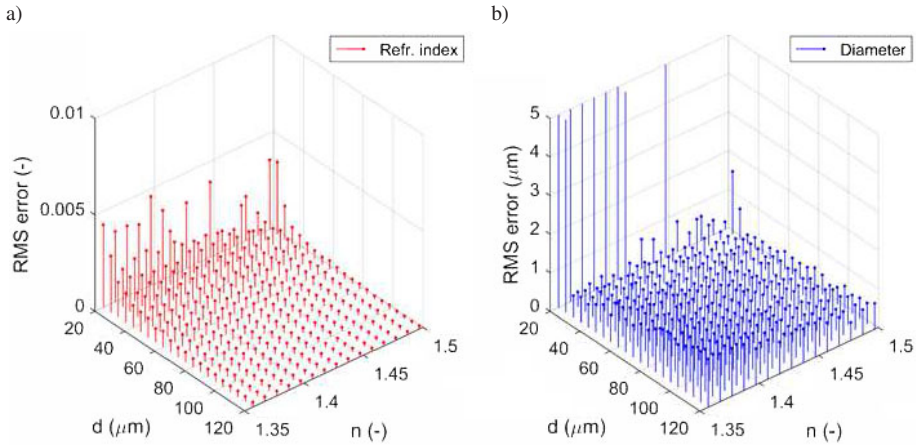


Fig. 11. The same as in Fig. 10 except that FWHM = 40 nm.

According to Fig. 10, the quality of diameter/refractive index estimates for very thin fibres ( $< 30 \mu\text{m}$ ) is rather poor, especially at high values of the refractive index. Fig. 2b helps to understand this issue: for very thin fibres the rainbow peaks are affected by some residual oscillations. The situation improves when the incident light is changed to a wider spectrum. According to Fig. 11, where FWHM = 40 nm, for 30–120  $\mu\text{m}$  thick silica fibres the diameter can be retrieved with an accuracy of 0.6% to 1.2%, while the refractive index can be specified with an uncertainty of  $\pm 1.2 \times 10^{-3}$  to  $\pm 1.7 \times 10^{-4}$ .

It is also worth noticing that the refractive index predictions are improved when the fibre's diameter increases. This is due to the fact that the Airy's function (6) provides more accurate results for the rainbow peak positions as the fibre size increases [38]. On the other hand, the diameter predictions become slightly worse as diameter increases. Noticing that the distance between rainbow peaks decreases as the fibre's diameter increases (in Fig. 2b), it is clear that the diameter predictions corresponding to the peak distance become less accurate due to limited peak position readings ( $0.005^\circ$ ).

## 5. Conclusions

Practical tests presented in this paper demonstrated that the rainbow method can be applied to non-contact measurements of transparent fibres, such as glass needles used in optically transparent fibrous reinforcements and optical fibres. Compared with the commercial "shadowgraph instruments" used in industry for the diameter monitoring and feedback control purposes, the rainbow method offers the possibility to characterize both refractive index and diameter. The use of a rather non-standard, polychromatic illumination suppresses noise and high-frequency features improving the accuracy of estimates. Simple formulas derived from the Airy's theory yield accurate results. Furthermore, the Airy's theory applied to the polychromatic beam scattering offers simplicity compared with the Mie theory, which is rigorous but unclear in its meaning.

## Acknowledgements

This work was supported by the Polish Ministry of Science and Higher Education, Project No. 049U/0087/19.

## References

- [1] Lin, H., Delbert, E.D., Stoffer, J.O. (1992). Optical and mechanical properties of optically transparent poly(methyl methacrylate) composites. *Polymer Engineering and Science*, 32, 344–350.
- [2] Desimone, D., Dlouhy, I., Lee, W.E., Koch, D., Horvath, J., Boccaccini, A. (2010). Optically-transparent oxide fibre-reinforced glass matrix composites. *Journal of Non-Crystalline Solids*, 356, 2591–2597.
- [3] Iba, H., Chang, T., Kagawa, Y. (2002). Optically transparent continuous glass fibre-reinforced epoxy matrix composite: fabrication, optical and mechanical properties. *Composites Science and Technology*, 62, 2043–2052.
- [4] Olson, J.R., Delbert, E.D., Stoffer, J.O. (1992). Fabrication and Mechanical Properties of an Optically Transparent Glass Fiber/Polymer Matrix Composite. *Journal of Composite Materials*, 26, 1181–1192.
- [5] Keaney, E., Shearer, J., Panwar, A., Mead, J. (2018). Refractive index matching for high light transmission composite systems. *Journal of Composite Materials*, 52, 3299–3307.
- [6] Onofri, F., Lenoble, A., Bultynck, H., Guéring, P.H. (2004). High-resolution laser diffractometry for the on-line sizing of small transparent fibres. *Optics Communications*, 234, 183–191.
- [7] Marshall, G.F. (2004). *Handbook of Optical and Laser Scanning*. New York: Marcel Dekker.
- [8] Mrocza, J. (2013). The cognitive process in metrology. *Measurement*, 46, 2896–2907.
- [9] Kisała, P., Harasim, D., Mrocza, J. (2016). Temperature-insensitive simultaneous rotation and displacement (bending) sensor based on tilted fiber Bragg grating. *Optics Express*, 24, 29922–29929.
- [10] Ciężczyk, S., Kisała, P., Mrocza, J. (2019). New Parameters Extracted from Tilted Fiber Bragg Grating Spectra for the Determination of the Refractive Index and Cut-Off Wavelength. *Sensors*, 19, 1964.
- [11] Adam, J.A. (2002). The mathematical physics of rainbows and glories. *Physics Reports*, 356, 229–365.
- [12] Laven, P. (2003). Simulation of rainbows, coronas, and glories by use of Mie Theory. *Applied Optics*, 42, 436–444.
- [13] Adam, J.A., Laven, P. (2007). Rainbows from inhomogeneous transparent spheres: a ray-theoretic approach. *Applied Optics*, 46, 922–929.
- [14] Fleming, J.W. (1984). Dispersion in GeO<sub>2</sub>-SiO<sub>2</sub> glasses. *Applied Optics*, 23, 4486–4493.
- [15] Kahnert, F.M. (2003). Numerical methods in electromagnetic scattering theory. *Journal of Quantitative Spectroscopy & Radiative Transfer*, 79–80, 775–824.
- [16] Bohren, C.F., Huffman, D.R. (1983). *Absorption and Scattering of Light by Small Particles*. New York: John Wiley & Sons.
- [17] Aden, A.L. (1951). Electromagnetic Scattering from Spheres with Sizes Comparable to the Wavelength. *Journal of Applied Physics*, 22, 601–605.
- [18] Können, G.P., de Boer, J.H. (1979). Polarized rainbow. *Applied Optics*, 18, 1961–1965.
- [19] Świrniak, G., Mrocza, J. (2016). Approximate solution for optical measurements of the diameter and refractive index of a small and transparent fiber. *Journal of the Optical Society of America A*, 33, 667–676.

- [20] Ashkin, A., Dziedzic, J.M. (1981). Observation of optical resonances of dielectric spheres by light scattering. *Applied Optics*, 20, 1803–1814.
- [21] Chýlek, P., Kiehl, J.T., Ko, M.K.W. (1978). Narrow resonance structure in the Mie scattering characteristics. *Applied Optics*, 17, 3019–3021.
- [22] Bertero, M., De Mol, C., Viano, G. (1980). The stability of inverse problems [in:] Baltes H.P. (eds.) *Inverse Scattering Problems in Optics. Topics in Current Physics*, 20, Berlin: Springer.
- [23] Devaney, A.J., Sherman, G.C. (1982). Nonuniqueness. in *Inverse Source and Scattering Problems. IEEE Transactions on Antennas and Propagation*, 30, 1034–1037.
- [24] Mroczka, J., Szczuczyński, D. (2010). Improved regularized solution of the inverse problem in turbidimetric measurements. *Applied Optics*, 49, 4591–4603.
- [25] Mroczka, J., Szczuczyński, D. (2012). Simulation research on improved regularized solution of inverse problem in spectral extinction measurements. *Applied Optics*, 51, 1715–723.
- [26] Mroczka, J., Szczuczyński, D. (2013). Improved technique of retrieving particle size distribution from angular scattering measurements. *Journal of Quantitative Spectroscopy and Radiative Transfer*, 129, 48–59.
- [27] Onofri, F., Krzysiek, M., Barbosa, S., Messenger, V., Ren, K.F., Mroczka, J. (2011). Near-critical-angle scattering for the characterization of clouds of bubbles: particular effects. *Applied Optics*, 50, 5759–5769.
- [28] Onofri, F., Krzysiek, M., Mroczka, J. (2007). Critical angle refractometry and sizing of bubble clouds. *Optics Letters*, 32, 2070–2072.
- [29] Airy, G.B. (1838). On the intensity of light in the neighbourhood of a caustic. *Transactions of the Cambridge Philosophical Society*, 6, University Press, 379.
- [30] Abramowitz, M., Stegun, I.A. (1970). *Handbook of Mathematical Functions*. 9th ed. Washington DC: National Bureau of Standards.
- [31] Nussenzweig, H.M. (1969). High-Frequency Scattering by a Transparent Sphere. II. Theory of the Rainbow and the Glory. *Journal of Mathematical Physics*, 10, 125–176.
- [32] Świrniak, G., Głomb, G. (2017). A tunable fiber-optic LED illumination system for non-invasive measurements of the characteristics of a transparent fiber. *Proc. of SPIE, Modeling Aspects in Optical Metrology VI*, 10330, 1033019.
- [33] Mroczka, J. (1988). Temperature stabilisation of light-emitting diode radiation. *Journal of Physics E: Scientific Instruments*, 21, 306–309.
- [34] Świrniak, G., Głomb, G. (2019). Experimental light scattering by optical fibers: system design and testing. *Proc. of SPIE, Optical Measurement Systems for Industrial Inspection XI*, 11056, 110563X–1.
- [35] Schubert, M.F., Chajed, S., Kim, J.K., Schubert, E.F. (2007). Polarization of light emission by 460nm GaInN/GaN light-emitting diodes grown on (0001) oriented sapphire substrates. *Applied Physics Letters*, 91, 051117–1.
- [36] Nussenzweig, H.M. (1992). *Diffraction Effects in Semiclassical Scattering*. Montroll Memorial Lecture Series in Mathematical Physics: 1. Cambridge: Cambridge University Press.
- [37] Berry, M.V., Upstill, C. (1980). Catastrophe optics: morphologies of caustics and their diffraction patterns. *Progress in Optics*, E. Wolf, ed. Amsterdam: Elsevier, 257–346.
- [38] Wang, R.T., van de Hulst, H.C. (1991). Rainbows: Mie computations and the Airy approximation. *Applied Optics*, 30, 106–117.